▌**Metal–Organic Frameworks**

# Engineered Bifunctional Luminescent Pillared-Layer Frameworks for Adsorption of $CO_2$ and Sensitive Detection of Nitrobenzene in Aqueous Media

Chun-Hao Su, Meng-Jung Tsai, Wei-Kai Wang, Yi-Yun Li, and Jing-Yun Wu*[a]

**Abstract:** Through a dual-ligand synthetic approach, five isoreticular primitive cubic (pcu)-type pillared-layer metal–organic frameworks (MOFs), [Zn₂(dicarboxylate)₂(NI-bpy-44)]·$x$DMF·$y$H₂O, in which dicarboxylate = 1,4-bdc (**1**), Br-1,4-bdc (**2**), NH₂-1,4-bdc (**3**), 2,6-ndc (**4**), and bpdc (**5**), have been engineered. MOFs **1–5** feature twofold degrees of interpenetration and have open pores of 27.0, 33.6, 36.8, 52.5, and 62.1%, respectively. Nitrogen adsorption isotherms of activated MOFs **1′–5′** at 77 K all displayed type I adsorption behavior, suggesting their microporous nature. Although **1′** and **3′–5′** exhibited type I adsorption isotherms of $CO_2$ at 195 K, MOF **2′** showed a two-step gate-opening sorption isotherm of $CO_2$. Furthermore, MOF **3′** also had a significant influence of amine functions on $CO_2$ uptake at high temperature due to the $CO_2$–framework interactions. MOFs **1–5** revealed solvent-dependent fluorescence properties; their strong blue-light emissions in aqueous suspensions were efficiently quenched by trace amounts of nitrobenzene (NB), with limits of detection of 4.54, 5.73, 1.88, 2.30, and 2.26 μM, respectively, and Stern–Volmer quenching constants ($K_{sv}$) of $2.93 \times 10^3$, $1.79 \times 10^3$, $3.78 \times 10^3$, $4.04 \times 10^3$, and $3.21 \times 10^3$ $M^{-1}$, respectively. Of particular note, the NB-included framework, NB@**3**, provided direct evidence of the binding sites, which showed strong host–guest π–π and hydrogen-bonding interactions beneficial for donor–acceptor electron transfer and resulting in fluorescence quenching.

## Introduction

Metal–organic frameworks (MOFs), constructed from metal ions/clusters as nodes and organic bridging ligands as linkers, have emerged as a fascinating class of crystalline porous materials in recent decades. MOFs usually have unique intriguing networks with essentially permanent porosity, making them useful platform candidates for wide application in gas storage and separation;[1,2] organic pollutant removal and degradation;[3,4] and, if suitably active or catalytic sites are available, catalysts and catalyst supports.[5] In addition, MOFs equipped with intrinsic luminescence properties are of particular interest, owing to their promising potential in hazardous chemical-sensing applications,[6,7] such as nitroaromatic compounds (NACs),[8–13] heavy-metal ions,[11–15] anions,[8,15–17] and volatile organic compounds (VOCs).[15,18]
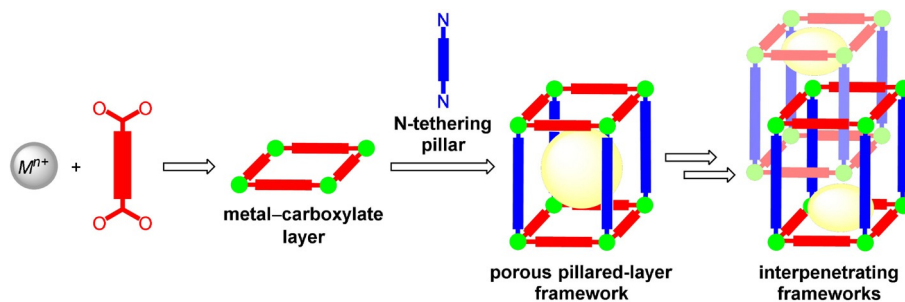
From a topological point of view, a pillared-layer MOF is usually composed of 2D metal–carboxylate layered nets and (rigid) linear bis-pyridyl N-tethering pillars.[19–25] Hence, the formation of (luminescent) isoreticular pillared-layer MOFs can be reasonably achieved by applying a dual-ligand synthetic approach (Scheme 1),[19] which is an alternative and effective approach to generate well-designed porous frameworks with adjustable pore sizes and tunable structural features by simply adjusting the length of the linear bis-pyridyl pillars[20–22,26] or by changing the polycarboxylate moieties.[23,24,27] Of particular note, as the length of the bridging ligands is increased, MOFs usually possess network interpenetration, which tends to diminish the porosity.[19,25] However, these (luminescent) isoreticular pillared-layer frameworks are essentially still porous and, hence, are capable of adsorbing small molecules. Nevertheless, it is not unreasonable to obtain other nonpillared-layer networks, owing to the unpredictable self-assembly process.

Herein, we report on the synthesis and structures of five zinc-based luminescent MOFs **1–5**, all of which adopt a pillared-layer open framework with a $4^{12}6^3$ topology (primitive cubic (pcu)-type) with a high porosity of approximately 27.0–62.1% sufficient free volumes. With the open framework and free void volumes in mind, thermally activated materials of MOFs **1–5** show significant $CO_2$ uptake capacities of 111.9–45.7 cm³ g⁻¹ at 195 K and $P/P_0 = 1$. Furthermore, MOFs **1–5** display solvent-dependent luminescence properties in different solvent suspensions, with the greatest fluorescence enhancement for aqueous suspensions, but the greatest fluorescence quenching for nitrobenzene (NB). Therefore, MOFs **1–5** are promising as potential fluorescence sensor materials for efficient, sensitive, and selective detection of trace amounts of NB from water. More interestingly, the as-obtained NB-included framework, NB@**3**, provides direct evidence for adsorbent–adsorbate (host–guest) π–π and hydrogen-bonding interactions

[a] C.-H. Su, Dr. M.-J. Tsai, W.-K. Wang, Y.-Y. Li, Prof. Dr. J.-Y. Wu
Department of Applied Chemistry, National Chi Nan University
Nantou 545 (Taiwan)
E-mail: jyunwu@ncnu.edu.tw

**Chemistry–A European Journal**

Full Paper
doi.org/10.1002/chem.202005373

**Chemistry Europe**
European Chemical
Societies Publishing

**Scheme 1.** Dual-ligand synthetic approach to pillared-layer MOFs.

between the framework and the nitro analyte, which result in a significant fluorescence quenching effect.

## Results and Discussion

### Ligand design

Naphthalimide (NI) derivatives with a large, planar, π-conjugated arene core(s) are attractive fluorophores in optoelectronics due to their adjustable photoluminescence properties through substitute modifications.[28–30] Upon immobilization with donating functions, such as pyridine and carboxyl, the highly emissive properties of NI derivatives encourage their use in the construction of luminescent MOFs as potential sensor materials.[24,31–33] Therefore, we have designed a NI-based bis-pyridyl ligand, namely, N-(pyridin-4-yl)-4-(pyridin-4-yl)-1,8-naphthalimide (NI-bpy-44),[24] with remarkable fluorescence as a potential provider of luminescence properties in isoreticular pillared-layer MOFs of various aromatic dicarboxylic acids (Scheme 2).
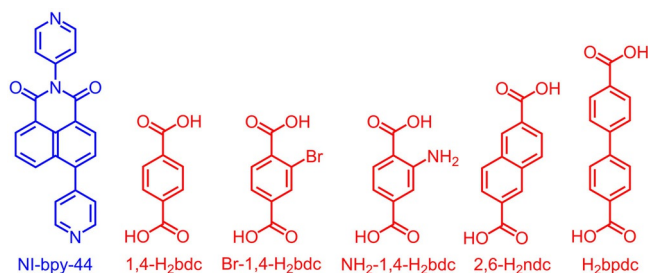


**Scheme 2.** Molecular structures of NI-bpy-44 and aromatic dicarboxylic acids.

### Synthesis and structures

Through a dual-ligand synthetic approach, pillared-layer MOFs [Zn$_2$(1,4-bdc)$_2$(NI-bpy-44)]·2.5 DMF·1.25 H$_2$O (**1**), [Zn$_2$(Br-1,4-bdc)$_2$(NI-bpy-44)]·2.5 DMF·2.25 H$_2$O (**2**), [Zn$_2$(NH$_2$-1,4-bdc)$_2$(NI-bpy-44)]·3 DMF·2 H$_2$O (**3**), [Zn$_2$(2,6-ndc)$_2$(NI-bpy-44)]·5 DMF·6.5 H$_2$O (**4**), and [Zn$_2$(bpdc)$_2$(NI-bpy-44)]·6 DMF·8.5 H$_2$O (**5**) have been engineered from the reactions of Zn(NO$_3$)$_2$·6 H$_2$O or ZnSO$_4$·7 H$_2$O, NI-bpy-44, and benzene-1,4-dicarboxylic acid (1,4-H$_2$bdc), 2-bromobenzene-1,4-dicarboxylic acid (Br-1,4-H$_2$bdc), 2-aminobenzene-1,4-dicarboxylic acid (NH$_2$-1,4-H$_2$bdc), naph-

thalene-2,6-dicarboxylic acid (2,6-H$_2$ndc), and biphenyl-4,4′-dicarboxylic acid (H$_2$bpdc), respectively, in a 2:1:2 ratio in DMF-only, DMF/H$_2$O, or DMF/CH$_3$OH solutions under hydro(solvo)-thermal conditions. It is reasonable to assign DMF and H$_2$O as the included lattice solvent molecules, the approximate quantities of which were determined by the residual electron densities in the framework voids squeezed from the single-crystal XRD data (see details in the experimental section in the Supporting Information).

From single-crystal X-ray structure analyses, the five Zn MOFs crystallized in the monoclinic space groups C2/m for **1** and C2/c for **2** and **3**, as well as triclinic space group P1̄ for **4** and **5**. For MOFs **1**–**5**, their frameworks are all composed of dinuclear [Zn$_2$(COO)$_4$)] paddlewheel secondary building units (SBUs), which are connected by aromatic dicarboxylate dianions to form a 2D square/rhombohedral grid of [Zn$_2$(dicarboxylate)$_2$]$_n$ (Figure S2 in the Supporting Information). The two remaining apical coordination sites of the paddlewheel [Zn$_2$(COO)$_4$] SBUs are occupied by ditopic NI-bpy-44 ligands as N-tethering pillars to demonstrate the formation of 3D open structures, so-called pillared-layer frameworks (Figure 1a). The topology of the frameworks in **1**–**5** can be best described as an elongated primitive cubic (pcu) lattice (Figure 1a), which has a point symbol of 4$^{12}$6$^3$. Two identical pillared-layer frameworks are mutually interpenetrated with each other, to yield overall doubly interpenetrating 3D frameworks (Figure 1b). Even if double interpenetration of the 3D frameworks, MOFs **1**–**5** show 1D open channels with dimensions of about 4.1×4.1 Å$^2$ along the [001] direction and about 2.7× 3.8 Å$^2$ along the [100] direction in **1**, about 2.5×2.5 Å$^2$ along the [101] direction and about 3.5×3.9 Å$^2$ along the [001] direction in **2**, about 3.4×3.4 Å$^2$ along the [101] direction and about 3.7×3.9 Å$^2$ along the [001] direction in **3**, about 2.6×6.6 and 3.5×5.9 Å$^2$ along the [001] direction and about 3.8×3.8 Å$^2$ along the [010] direction in **4**, and about 2.1×6.8 and 4.0× 5.4 Å$^2$ along the [001] direction and about 4.6×5.3 Å$^2$ along the [100] direction in **5**. As a consequence, MOFs **1**–**5** have sufficient free volumes of 27.0, 33.6, 36.8, 52.5, and 62.1 %, respectively, as calculated by the PLATON routine.[34] Notably, even upon increasing the lengths of the dicarboxylate ligands from 1,4-bdc$^{2-}$ (6.8 Å) to 2,6-ndc$^{2-}$ (9.0 Å) and then to bpdc$^{2-}$ (11.0 Å), the overall frameworks for MOFs **1**–**5** retain twofold degrees of interpenetration, and thus, the free volumes increase significantly.
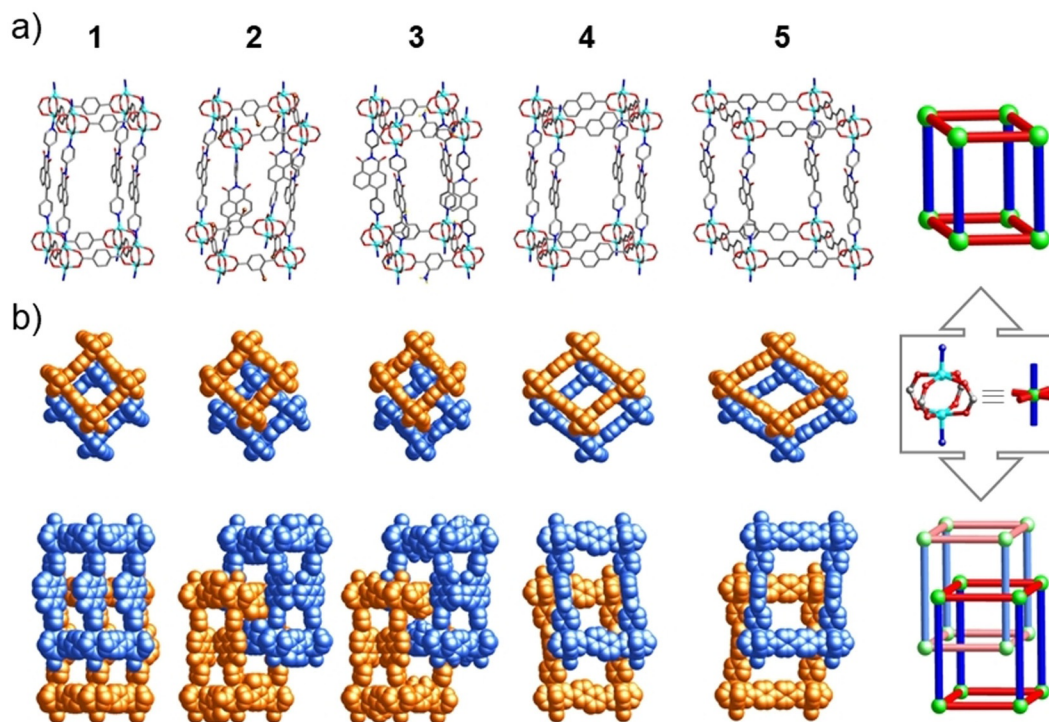
**Figure 1.** Crystal structures and schematic representations of MOFs [Zn$_2$(dicarboxylate)$_2$(NI-bpy-44)]·$x$DMF·$y$H$_2$O (**1**–**5**): a) a single pcu-type pillared-layer open framework and b) top and side views of doubly interpenetrating frameworks.

## Phase purity and thermal stability

Powder X-ray diffraction (XRPD) measurements showed that the experimental XRPD patterns of **1**–**5** closely matched with those of the computer-simulated one generated from the single-crystal structure determination (Figure S3 in the Supporting Information), confirming the bulk-phase purity. Notably, there are slight differences in intensity and in some peaks, which might be due to the influence of the preferred orientation and partial crystal packing distortion/collapse arising from the escape of lattice solvents before loading the sample for XRPD measurements and during the period of XRPD measurements. Thermal analyses of MOFs **1**–**5** were performed under a nitrogen atmosphere (Figure S4 in the Supporting Information). Prior to thermogravimetric (TG) measurements, the polycrystalline samples of MOFs **1**–**5** were immersed in methanol for 3 d and then collected by filtration and dried in air at room temperature. The TG curves of solvent-activated materials of MOFs **1**–**5** revealed a slight weight loss, due to moisture, before they began to decompose at temperatures approaching 327, 319, 307, 350, and 315 °C, respectively. The decomposition process ended upon heating to about 476, 597, 508, 460, and 524 °C, respectively, leaving the final residue of ZnO (for **1**: found: 20.3%; calcd: 20.6%; for **2**: found: 15.6%; calcd: 16.8%; for **3**: found: 19.0%; calcd: 19.4%; for **4**: found: 18.2%; calcd: 17.9%; for **5**: found: 16.7%; calcd: 16.7%).

## Gas adsorption

The pertinent porosities of MOFs **1**–**5** were examined by gas adsorption. Prior to the sorption measurements, the as-synthesized samples of MOFs **1**–**5** were exchanged with methanol and subsequently degassed at 373 K under high vacuum for 24 h. The as-obtained activated materials of MOFs **1**–**5** are termed **1**′–**5**′ hereafter. Reports in the literature have shown that MOF structures build of only paddlewheel [Zn$_2$(COO)$_4$)] SBUs are highly sensitive and easily collapse in air.[35] To examine the stability of activated MOFs **1**′–**5**′, XRPD measurements were conducted. After activation, the XRPD patterns of **1**′–**5**′ are similar to simulated and as-synthesized XRPD patterns of pristine **1**–**5** (Figure S3 in the Supporting Information), ensuring that their frameworks were still intact, to a certain extent.

For **1**′–**5**′, low-pressure physisorption experiments of N$_2$ were conducted at 77 K, which showed type I adsorption isotherms in all cases (Figure 2 a), suggesting their microporous nature. The N$_2$ uptakes for **4**′ and **5**′ are sharply increased at $P/P_0 > 0.94$, mostly due to the capillary condensation process.[36] As a result, the maximum uptakes of N$_2$ are about 105, 48, 56, 20, and 29 cm$^3$ g$^{-1}$ for **1**′–**5**′, respectively. Accordingly, the BET surface areas for **1**′–**5**′ are estimated to be 259, 137, 157, 44, and 36 m$^2$ g$^{-1}$, respectively. On the other hand, CO$_2$ adsorption–desorption isotherms for **1**′–**5**′ were recorded volumetrically at 195, 273, and 298 K. The CO$_2$ adsorption profiles of **1**′–**5**′ all are typical type I adsorption isotherms, with the exception of **2**′ at 195 K (Figure 2 b). As observed, the CO$_2$ adsorption profile of **2**′ at 195 K exhibits a two-step sorption at a pressure of about $P/P_0 \approx 0.48$ (the gate-opening pressure) with an
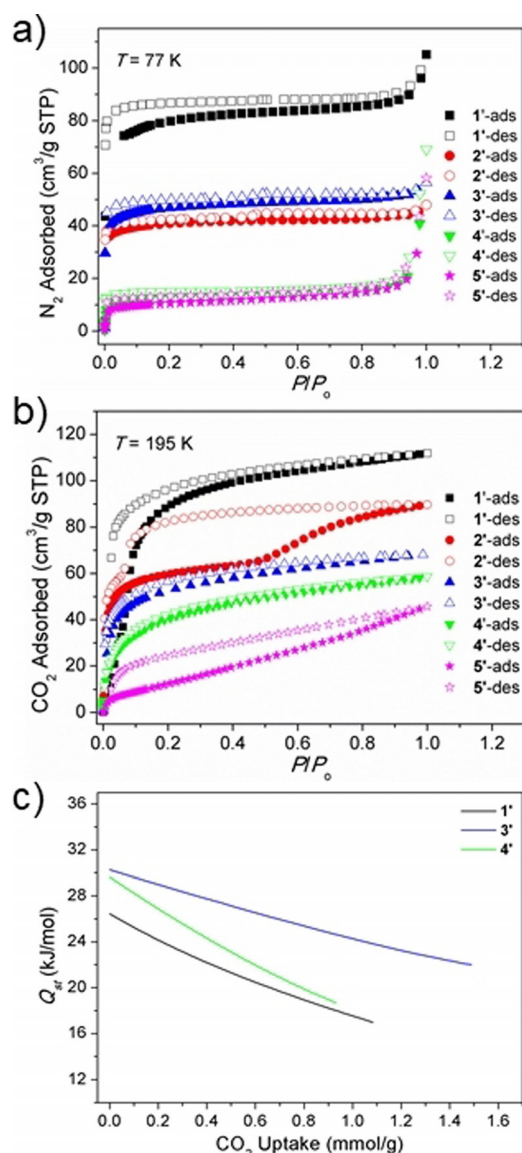
**Chemistry–A European Journal**

Full Paper
doi.org/10.1002/chem.202005373

**Chemistry Europe**
European Chemical
Societies Publishing

**Figure 2.** a) Nitrogen adsorption isotherms of evacuated MOFs **1′**–**5′** at 77 K. b) $CO_2$ adsorption isotherms of evacuated MOFs **1′**–**5′** at 195 K. c) The isosteric heat ($Q_{st}$) of $CO_2$ adsorption for **1′**, **3′**, and **4′**.

$CO_2$ is about 111 $cm^3 g^{-1}$ (4.95 $mmol\,g^{-1}$) for **1′**, 89 $cm^3 g^{-1}$ (3.97 $mmol\,g^{-1}$) for **2′**, 68 $cm^3 g^{-1}$ (3.04 $mmol\,g^{-1}$) for **3′**, 58 $cm^3 g^{-1}$ (2.59 $mmol\,g^{-1}$) for **4′**, and 45 $cm^3 g^{-1}$ (2.01 $mmol\,g^{-1}$) for **5′** at 195 K and $P/P_0 = 1$, which are comparable with those of some reported paddlewheel Zn MOFs (Table S2 in the Supporting Information).[40–53] At high temperature (Figure S5 in the Supporting Information), MOFs **1′**, **3′**, and **4′** exhibit significant $CO_2$ uptake at both 273 and 298 K, with capacities of 20–33 and 15–24 $cm^3 g^{-1}$, respectively; MOF **2′** reveals a significant $CO_2$ uptake of 22 $cm^3 g^{-1}$ at 273 K, but negligible uptake capacity at 298 K; MOF **5′** displays no $CO_2$ uptakes at both temperatures. On the basis of experimental isotherm data at 273 and 298 K, the isosteric heat ($Q_{st}$) of $CO_2$ adsorption could be calculated to evaluate the extent of $CO_2$–framework interactions.[54,55] The $Q_{st}$ values for **1′**, **3′**, and **4′** at zero loading are about 26.4, 30.2, and 29.6 $kJ\,mol^{-1}$, respectively, which decrease with increasing $CO_2$ uptakes (Figure 2 c). These values are higher than that of the enthalpy (17 $kJ\,mol^{-1}$) of liquefaction of $CO_2$,[56] reflecting a strong $CO_2$–framework interaction, that is, the adsorbate–adsorbent interaction. The gas adsorption properties of **1′**–**5′** are summarized in Table 1.

Herein, the $N_2$ (77 K) and $CO_2$ (195 K) uptakes for **1′** are both much higher than those for **2′** and **3′** with almost identical ligand lengths of benzene-1,4-dicarboxylates, whereas the BET value of **1′** is greater than those of **2′** and **3′**. Such results can be reasonably attributed to the presence of bromo and amine substitutes in **2′** and **3′**, respectively; the increase in steric hindrance of the bulky substitutes on benzene-1,4-dicarboxylate ligands in channels significantly narrows the channels and reduces the pore volumes. On the other hand, upon increasing the ligand length from 1,4-bdc$^{2-}$ (6.8 Å) in **1′** to 2,6-ndc$^{2-}$ (9.0 Å) in **4′** and then bpdc$^{2-}$ (11.0 Å) in **5′**, the sufficient free volumes increase significantly from 27.0 (**1′**) to 52.5% (**4′**) and then 62.1% (**5′**). Nevertheless, the uptake amounts of $N_2$ at 77 K and $CO_2$ at 195 K for **4′** and **5′** fell short of our expectations; the capacities were less than 50% of that of **1′**. From a structural point of view, MOFs **4′** and **5′** show compressed rhombohedral pores, rather than regular square pores, such as those in **1′**–**3′**, suggesting small pore windows and maybe structural flexibility. This implies that a framework slip and/or structural distortion might take place during activation to result in pore narrowing or pore closing. The very tiny differences between the XRPD patterns of as-synthesized **4** and **5** and activated **4′** and **5′** support such possibilities (Figure S3 d and e in the Supporting Information). Therefore, the relatively low $N_2$ and $CO_2$ uptakes for **4′** and **5′** are tentatively explained by acti-

uptake of about 65 $cm^3 g^{-1}$ (2.90 $mmol\,g^{-1}$), suggesting gate-opening-type behavior.[37–39] Moreover, the desorption part of the isotherm does not trace the adsorption process, but a two-step desorption occurs at $P/P_0 \approx 0.06$ (gate-closing pressure), resulting in a strong hysteresis loop. The maximum uptake of

**Table 1.** Gas adsorption properties of **1′**–**5′**.

| MOF | Voids [%] | $N_2$ uptakes at 77 K [$cm^3\,g^{-1}$ STP] | $S_{BET}$ [$m^2\,g^{-1}$] | $CO_2$ uptake ($cm^3 g^{-1}$ STP) 195 K | 273 K | 298 K | $-Q_{st}(CO_2)$ [$kJ\,mol^{-1}$] |
|---|---|---|---|---|---|---|---|
| **1′** | 27.0 | 105 | 259 | 111 | 24 | 16 | 26.4 |
| **2′** | 33.6 | 48 | 137 | 89 | 22 | 3 | n.a.[a] |
| **3′** | 36.8 | 56 | 157 | 68 | 33 | 24 | 30.2 |
| **4′** | 52.5 | 20 | 44 | 58 | 20 | 15 | 29.6 |
| **5′** | 62.1 | 29 | 36 | 45 | 0.8 | 0.5 | n.a.[a] |

[a] n.a. = not available.

**Chemistry–A European Journal**

Full Paper
doi.org/10.1002/chem.202005373

**Chemistry Europe**
European Chemical
Societies Publishing

vation- and sorption-induced framework distortions. Furthermore, there is an abrupt decrease of $CO_2$ adsorption for **1′–5′** at 273 K compared with that at 195 K. This indicates that **1′–5′** might experience framework distortion at enhanced temperatures, resulting in surface adsorption and/or no inclusion in the pores.[37]

Additionally, MOF **3′** reveals the highest $CO_2$ adsorption capacity among the five isostructural analogues at high temperature (273 and 298 K). This can be interpreted by the influence of the amine functions bound to the aromatic dicarboxylate ligands as chemically reactive adsorption sites,[56–62] which offer dipole–quadruple interactions and/or N–H···O hydrogen-bonding interactions to strongly interact with $CO_2$ molecules.[56–60] The $Q_{st}$ value for **3′**, which contains amine-functionalized 1,4-bdc ligands, is at least 4 kJ mol$^{-1}$ greater than that for **1′**, which has naked 1,4-bdc ligands, across all loadings, suggesting stronger interactions between the functionalized frameworks and $CO_2$, and thus, providing direct proof of the enhanced $CO_2$ binding affinity of **3′** that has a significant, positive effect on the adsorption of $CO_2$.[53]

## Fluorescent properties

The solid-state fluorescent properties of MOFs **1–5**, NI-bpy-44, and aromatic dicarboxylic acids (1,4-$H_2$bdc, Br-1,4-$H_2$bdc, $NH_2$-1,4-$H_2$bdc, 2,6-$H_2$ndc, and $H_2$bpdc) were investigated at room temperature (Figure S6 in the Supporting Information). The NI-bpy-44 ligand showed a broadened emission band centered at 429 nm if it was excited at $\lambda_{ex} = 280$ nm. On the other hand, 1,4-$H_2$bdc, Br-1,4-$H_2$bdc, $NH_2$-1,4-$H_2$bdc, and $H_2$bpdc all revealed emission bands with maxima at 381 ($\lambda_{ex} = 280$), 392 (245), 544 (370), and 406 nm (275 nm), respectively, whereas 2,6-$H_2$ndc exhibited two emission bands centered at 404 and 422 nm ($\lambda_{ex} = 280$ nm). The emissions are most likely ascribed to the π*→π and/or π*→n transitions.[24,33,63,64] For MOFs **1–5**, similar solid-state fluorescence spectra were observed upon excitation, showing a blue/cyan emission band centered at 425 nm ($\lambda_{ex} = 280$ nm) for **1**, 424 nm ($\lambda_{ex} = 280$ nm) for **2**, 445 nm ($\lambda_{ex} = 370$ nm) for **3**, 460 nm ($\lambda_{ex} = 280$ nm) for **4**, and 465 nm ($\lambda_{ex} = 280$ nm) for **5**. Based on the similarities of band positions and shapes, the emission bands for **1–5** are tentatively attributed to the ligand-centered emission, which mostly arises from NI-bpy-44.[24]

The luminescence responses of MOFs **1–5** dispersed in various kinds of solvents, such as $H_2O$, methanol, acetonitrile, dichloromethane, toluene, DMF, and NB, were further investigated in suspension. The finely ground powders (1 mg) of MOFs **1–5** were dispersed in water and selected organic solvents (3 mL), followed by ultrasonic agitation for 30 min, and then corresponding photoluminescence spectra were recorded. MOFs **1–5** in different solvent suspensions displayed strong guest-dependent luminescence properties (Figure S7 in the Supporting Information). The luminescent intensities of MOFs **1–5** were strongly dependent on the identities of the organic solvent molecules (Figure 3). As representative examples, aqueous suspensions of MOFs **1–5** exhibited the most remarkable luminescence intensity enhancements, among these solvent
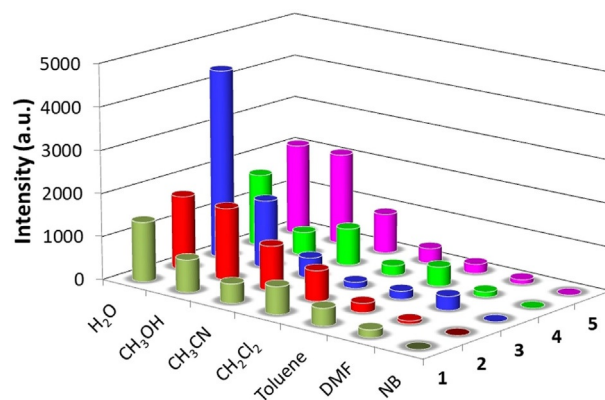


**Figure 3.** Bar diagram showing the maximal emission intensities of MOFs **1–5** in different solvent suspensions.

suspensions, whereas their NB suspensions revealed the most significant quenching effects, followed by DMF suspensions, to display significant luminescence intensity reductions. For other solvent molecules, such as $CH_3OH$, $CH_3CN$, $CH_2Cl_2$, and toluene, as the dispersion media, MOFs **1–5** showed luminescent intensities from moderate to weak. Such phenomena can be mainly attributed to different interactions between the homogeneously dispersible framework structure and distinct solvent molecules.[65,66] On the other hand, shifts in the luminescence emissions of MOFs **1–5** were observed upon changing the solvent, with the longest luminescence band appearing in the case of toluene ($\lambda_{em} = 446$–460 nm). Comparably, the positions of the luminescence bands of MOFs **1–5** in other solvent suspensions are blueshifted by about 30–60 nm.

## Fluorescence sensing of NB

MOFs **1–5** emitted strong blue/cyan fluorescence in aqueous suspensions, but no fluorescence in NB suspensions. In addition, MOFs **1–5** showed high aqueous stability, as supported by XRPD patterns, which gave almost unchanged profiles compared with those of the as-synthesized ones after immersion in water for 7 d (Figure S3 in the Supporting Information). These features make them promising fluorescence probes for the convenient and sensitive detection of trace amounts of NB in water. To gain a deeper insight into the sensing sensitivity towards NB for MOFs **1–5**, fluorescent titration experiments were investigated through gradually increasing the concentrations of NB in aqueous suspensions of MOFs **1–5**, and then the emissive responses were recorded (Figure 4 and Figure S8 in the Supporting Information). As observed, the fluorescence intensity decreases with an increase of the volumetric concentration of NB, indicating diffusion-controlled fluorescence quenching.[65,67] The percentage of quenching is defined as $(I_0-I)/I_0 \times 100\%$, in which $I_0$ and $I$ denote the fluorescence intensities before and after the addition of NB, respectively. As a representative example, the percentage of quenching quickly increased in the early stage with NB concentrations in the range of about 0–0.4 mM for **1** and **5**, 0–0.3 mM for **3** and **4**, and 0–0.7 mM for **2** (Figure S9 in the Supporting Information), which

Chemistry–A European Journal

Full Paper
doi.org/10.1002/chem.202005373

**Chemistry Europe**
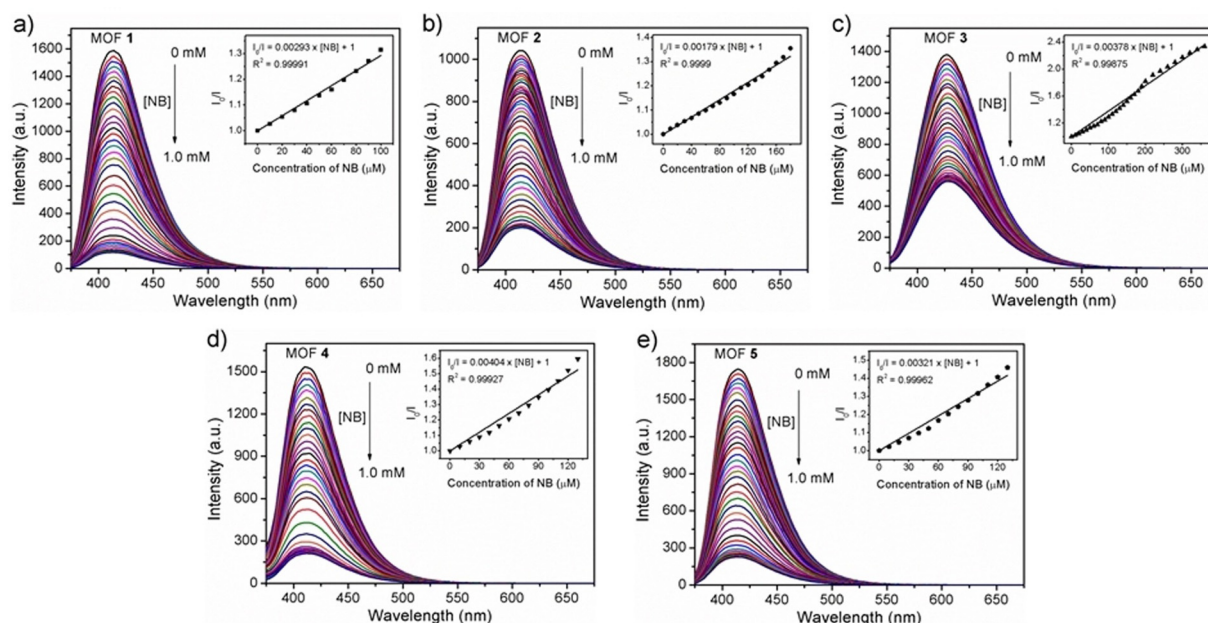European Chemical
Societies Publishing

**Figure 4.** Emission spectra of MOFs **1–5** (a–e) dispersed in water with the gradual addition of NB upon excitation at 350 nm. Inset: Linear Stern–Volmer plot of NB.

then gradually reached a maximum of approximately 92% at 0.55 mM for **1**, 80% at 0.75 mM for **2**, 59% at 0.65 mM for **3**, 85% at 0.50 mM for **4**, and 87% at 0.70 mM for **5**. According to the quenching efficiency, it is clear that MOFs **1**, **4**, and **5** revealed high quenching rates and quenching percentages, and thus, are potentially good sensor materials. Comparably, MOF **2** showed the slowest quenching rate among the five analogues, but a high percentage of quenching, whereas MOF **3** displayed a high quenching rate, but the lowest value of percentage of quenching, indicating a relatively poor sensor material. These phenomena might be attributed to the influences of bromo and amino substitutions on the 1,4-bdc ligands in **2** and **3**, respectively.

The quenching efficiency can also be quantitatively analyzed by a Stern–Volmer analysis based on the equation $I_0/I = 1 + K_{sv}[Q]$, in which $I_0$ and $I$ denote the fluorescence intensities before and after the addition of NB, respectively; $K_{sv}$ is the Stern–Volmer quenching constant ($M^{-1}$), and $[Q]$ is the concentration of NB (mM). The Stern–Volmer plots for MOFs **1–5** in water upon incremental addition of NB over the entire range of test concentrations (0–1.0 mM) showed a deviation from a straight line with upward curvature, followed by quenching reaching a constant extent in the high-concentration range (Figure S10 in the Supporting Information). This clearly specifies that the quenching process was caused by the cooperation of a dynamic energy-transfer quenching mechanism, owing to collisions of NB molecules with the framework surface of MOFs **1–5**, and a static self-absorption quenching mechanism,[8,17,68,69] and there are limited accessible binding sites on the framework surfaces of MOFs **1–5** that could be in close contact with NB.[31] The $K_{sv}$ estimated from the linearity of $I_0/I$ versus [NB] gave a value of $2.93 \times 10^3\,M^{-1}$ in 0–100 μM ($R^2 = 0.99991$) for **1**, $1.79 \times 10^3\,M^{-1}$ in 0–180 μM ($R^2 = 0.9999$) for **2**,

$3.78 \times 10^3\,M^{-1}$ in 0–360 μM ($R^2 = 0.99875$) for **3**, $4.04 \times 10^3\,M^{-1}$ in 0–130 μM ($R^2 = 0.99927$) for **4**, and $3.21 \times 10^3\,M^{-1}$ in 0–130 μM ($R^2 = 0.99962$) for **5** (Figure 4, insets), suggesting a strong quenching effect on fluorescence. The values are comparable with those reported for MOF-based sensor materials in the literature (Table S3 in the Supporting Information).[8–10,13,33,70–71] On the other hand, the detection sensitivity of MOFs **1–5** toward NB could be determined by the limit of detection (LOD), by using the equation LOD = $3\sigma/k$, in which $\sigma$ is the standard deviation from five blank measurements and $k$ is the absolute value of the slope of the calibration curve at lower concentrations. According to fluorescence measurements with NB concentrations of 0–0.10 mM, the LODs of MOFs **1–5** dispersed in $H_2O$ for the detection of NB were estimated to be 4.54, 5.73, 1.88, 2.30, and 2.26 μM in sequence (Figure S11 in the Supporting Information), revealing a very high sensitivity for NB detection.

The recyclability of MOFs **1–5** for the detection of NB has further been explored (Figure 5). Experimental results showed that the recovered powdered samples of MOFs **1–5** returned their fluorescence to approximately 90% intensity after five consecutive sensing–regeneration runs. Furthermore, MOFs **1–5** also displayed high activity in turn-off fluorescent sensing toward NB with a negligible reduction in quenching efficiency. These results imply that MOFs **1–5** have remarkable long-term activity and stability as reusable fluorescence sensors in the detection of NB in water.

With the aim of practical applications, we attempted to prepare thin-film-based devices for the detection of NB by MOFs **1–5** (Figure 6). As a representative example, with the exception of MOF **3**, which showed poor solid-state fluorescence, thin-film-based devices of four other MOFs all demonstrated good virtual detection toward NB with a concentration as low as
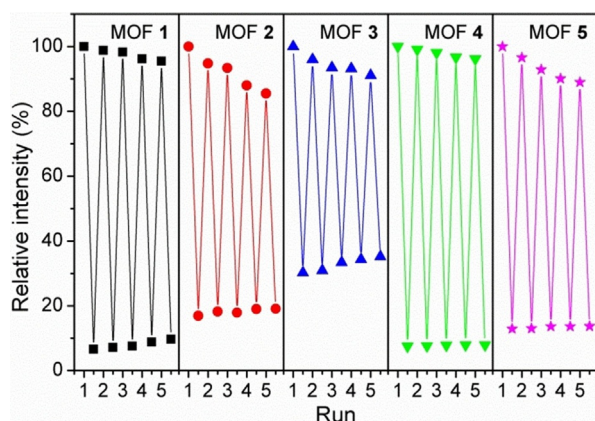
**Chemistry–A European Journal**

Full Paper
doi.org/10.1002/chem.202005373

**Chemistry Europe**
European Chemical
Societies Publishing

**Figure 5.** Recyclability of MOFs **1**–**5** for the fluorescence sensing of NB in water for five runs.
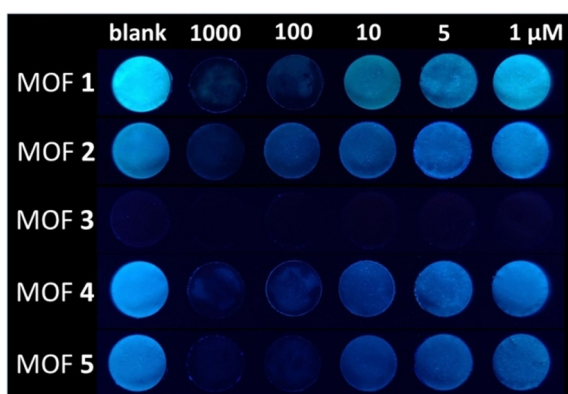


**Figure 6.** Photographs of thin-film-based devices for the virtual detection of NB in various concentrations by MOFs **1**–**5**.

5 μM, or maybe even lower. These values, notably, are very close to the LODs determined by spectroscopic methods.

To elucidate a possible mechanism for the observed turn-off fluorescence responses of MOFs **1**–**5** to NB, several examinations have been checked. It is first noted that MOFs **1**–**5**, after immersion in pure NB for 1 day, showed almost unchanged XRPD patterns compared with their as-synthesized XRPD patterns (Figure S3 in the Supporting Information), suggesting the maintenance of structural integrity. The high aqueous and NB stability of MOFs **1**–**5** imply that their frameworks after NB detection in water were intact, excluding framework collapse from fluorescence quenching responses for sensing NB. On the other hand, the UV/Vis absorption spectra of NB in aqueous solutions show no overlap with the emission profiles of MOFs **1**–**5** in water (Figure S12 in the Supporting Information). This provides clear evidence to rule out the long-range resonance energy-transfer process from the fluorophores of MOFs **1**–**5** to the nonemissive NB analyte.[72] Furthermore, the wavelength of irradiation light at $\lambda = 350$ nm indicates the negligible probability of competitive absorption for the quenching responses.[73] However, there is a preliminary consensus that the quenching effect can be mostly ascribed to the donor–acceptor electron-transfer mechanism.[10,13,73–75] Because a nitro group is a typical

electron-withdrawing substituent and stabilizes the LUMO of the aromatic analyte through conjugation,[75] NB is therefore highly electron deficient in nature and generally has a LUMO lying at a lower energy than that of the conduction band of a MOF.[9] Once NB is able to diffuse inside the channels of the host frameworks of MOFs **1**–**5**, the presence of the aromatic ring allows NB to form a close attachment to the interior walls of the frameworks and facilitate possible host–guest stacking interactions.[9,13] As a consequence, the excited electrons could easily transfer from the conduction band of the electron-donating frameworks to the low-lying LUMO of electron-deficient NB, resulting in a gradual decrease in fluorescence intensity.

## Inclusion of NB in pillared-layer frameworks

Of particular interest, the crystalline solids of **3** recovered from being soaked in neat liquid-phase NB displayed XRPD patterns that were almost in agreement with that of as-synthesized and simulated patterns (Figure S13 in the Supporting Information), suggesting maintenance of the crystal framework. More importantly, the shape and transparency of as-obtained crystals of **3** were mostly retained. Therefore, single-crystal XRD analysis was further performed for crystals of **3** after being soaked in neat liquid-phase NB. Fortunately, the collected diffraction data were sufficient to solve the structure of the as-obtained crystals, which were formulated to be [Zn$_2$(NH$_2$-1,4-bdc)$_2$(NI-bpy-44)]·NB·H$_2$O (NB@**3**), involving the inclusion of NB and H$_2$O molecules as lattice solvent molecules. Moreover, the IR spectra of NB@**3** clearly showed the inclusion of NB in the doubly interpenetrating frameworks of **3** (Figure S14 in the Supporting Information). The TG curve of NB@**3** showed 17.7% weight loss of included NB and H$_2$O molecules between room temperature and 208 °C (calcd: 14.3%) and a decomposition process between 302 and 537 °C (Figure S15 in the Supporting Information).

From single-crystal X-ray structure analyses, NB@**3** has cell parameters that are very close to those of **3** (Table S1 in the Supporting Information), both of them crystallized in monoclinic space group $C2/c$. The crystal structure of NB@**3** showed the inclusion of NB within the twofold interpenetrating frameworks of **3** (Figure 7a). As observed, the framework of **3** makes close contact with NB through pertinent host–guest N–H···O hydrogen-bonding interactions and π–π interactions (Figure 7b and c), confirming the encapsulation of NB in the open pores of the framework through solvent exchange through a single-crystal to single-crystal transformation.

Notably, the NB-included framework, NB@**3**, upon excitation at $\lambda_{ex} = 370$ nm, at room temperature showed a solid-state fluorescent emission band centered at 450 nm with a very weak intensity that was only approximately 5% of that of **3**, appearing about 95% quenching (Figure S16 in the Supporting Information). This is in agreement with the results of NB sensing of **3** in water. The crystal structure of NB@**3** may provide direct evidence of the detection sites. The strong adsorbent–adsorbate interactions between the aromatic NI moieties of the NI-bpy-44 ligand and the electron-deficient NB molecule may greatly benefit donor–acceptor electron transfer, resulting
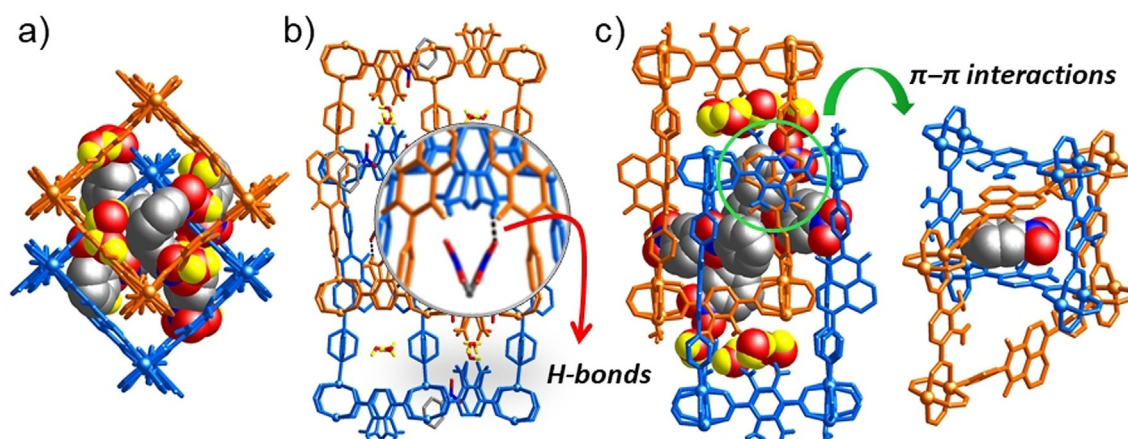
**Chemistry–A European Journal**

Full Paper
doi.org/10.1002/chem.202005373

**Chemistry Europe**
European Chemical
Societies Publishing

**Figure 7.** Crystal structure of NB@**3**: a) top view to show the inclusion of NB and $H_2O$ molecules (space-filling models) in the doubly interpenetrating frameworks of **3**; highlights of pertinent host–guest N–H···O hydrogen-bonding (b) and π–π interactions (c).

in a decrease in fluorescence intensity. One similar confirmation is observed for a 3D Li-based luminescent MOF, [Li$_3$\{Li(dmf)$_2$\}(cpma)$_2$]·4 DMF·H$_2$O ($H_2$CPMA = bis(4-carboxyphenyl)-$N$-methylamine), which shows a dramatic color change with concurrent luminescence quenching in the solid state for the selective detection of NB, as interpreted through the direct observation of interaction sites.[76]

## Conclusion

Herein, MOFs **1**–**5**, featuring twofold interpenetrating pcu-type pillared-layer frameworks, with sufficient free volumes of 27.0, 33.6, 36.8, 52.5, and 62.1%, respectively, have been hydro(solvo)thermally synthesized. $CO_2$ adsorption studies showed that thermally activated materials **1′**–**5′** displayed adsorption capacities of 111, 89, 68, 58, and 45 cm$^3$ g$^{-1}$ at 195 K and $P/P_0 = 1$, of which evacuated MOF **2′** exhibited a gate-opening effect and clear hysteresis phenomenon. MOFs **1**–**5** exhibited intense blue-light emissions in aqueous suspensions, which would be effectively quenched by NB. The quenching percentages, Stern–Volmer quenching constants ($K_{sv}$), and LOD values indicated that MOFs **1**–**5** would be good, recyclable, fluorescence sensor materials for the sensitive detection of NB. Moreover, thin-film-based fluorescence sensor devices for the detection of NB by MOFs **1**, **2**, **4**, and **5** would work properly, with remarkably low detection concentrations at the micromolar level, thus displaying excellent potential for practical applications. Most importantly, the NB-inclusion framework, NB@**3**, provided direct and clear evidence of adsorbent–adsorbate interactions between the framework surface and NB, which could facilitate electron transfer to lead to corresponding fluorescence quenching.

## Acknowledgements

## Conflict of interest

The authors declare no conflict of interest.

[1] C. A. Trickett, A. Helal, B. A. Al-Maythalony, Z. H. Yamani, K. E. Cordova, O. M. Yaghi, *Nat. Rev. Mater.* **2017**, *2*, 17045.
[2] H. Li, K. Wang, Y. Sun, C. T. Lollar, J. Li, H.-C. Zhou, *Mater. Today* **2018**, *21*, 108–121.
[3] E. M. Dias, C. Petit, *J. Mater. Chem. A* **2015**, *3*, 22484–22506.
[4] C.-C. Wang, J.-R. Li, X.-L. Lv, Y.-Q. Zhang, G. Guo, *Energy Environ. Sci.* **2014**, *7*, 2831–2867.
[5] L. Zhu, X.-Q. Liu, H.-L. Jiang, L.-B. Sun, *Chem. Rev.* **2017**, *117*, 8129–8176.
[6] W. P. Lustig, S. Mukherjee, N. D. Rudd, A. V. Desai, J. Li, S. K. Ghosh, *Chem. Soc. Rev.* **2017**, *46*, 3242–3285.
[7] S. A. Diamantis, A. Margariti, A. D. Pournara, G. S. Papaefstathiou, M. J. Manos, T. Lazarides, *Inorg. Chem. Front.* **2018**, *5*, 1493–1511.
[8] B. Parmar, Y. Rachuri, K. K. Bisht, R. Laiya, E. Suresh, *Inorg. Chem.* **2017**, *56*, 2627–2638.
[9] S. Srivastava, B. K. Gupta, R. Gupta, *Cryst. Growth Des.* **2017**, *17*, 3907–3916.
[10] Z. Sun, P. Hu, Y. Ma, L. Li, *Dyes Pigm.* **2017**, *143*, 10–17.
[11] S. Senthilkumar, R. Goswami, V. J. Smith, H. C. Bajaj, S. Neogi, *ACS Sustainable Chem. Eng.* **2018**, *6*, 10295–10306.
[12] L. Yang, C. Lian, X. Li, Y. Han, L. Yang, T. Cai, C. Shao, *ACS Appl. Mater. Interfaces* **2017**, *9*, 17208–17217.
[13] Y.-T. Yan, J. Liu, G.-P. Yang, F. Zhang, Y.-K. Fan, W.-Y. Zhang, Y.-Y. Wang, *CrystEngComm* **2018**, *20*, 477–486.
[14] R. Lv, H. Li, J. Su, X. Fu, B. Yang, W. Gu, X. Liu, *Inorg. Chem.* **2017**, *56*, 12348–12356.
[15] Y. Zhao, X. Xu, L. Qiu, X. Kang, L. Wen, B. Zhang, *ACS Appl. Mater. Interfaces* **2017**, *9*, 15164–15175.
[16] T. He, Y.-Z. Zhang, X.-J. Kong, J. Yu, X.-L. Lv, Y. Wu, Z.-J. Guo, J.-R. Li, *ACS Appl. Mater. Interfaces* **2018**, *10*, 16650–16659.
[17] X. Sun, S. Yao, C. Yu, G. Li, C. Liu, Q. Huo, Y. Liu, *J. Mater. Chem. A* **2018**, *6*, 6363–6369.

[18] X. Zheng, R. Fan, Y. Song, A. Wang, K. Xing, X. Du, P. Wang, Y. Yang, *J. Mater. Chem. C* **2017**, *5*, 9943–9951.

[19] C.-H. Lee, J.-Y. Wu, G.-H. Lee, S.-M. Peng, J.-C. Jiang, K.-L. Lu, *Cryst. Growth Des.* **2014**, *14*, 5608–5616.

[20] B. Chen, S. Ma, F. Zapata, F. R. Fronczek, E. B. Lobkovsky, H.-C. Zhou, *Inorg. Chem.* **2007**, *46*, 1233–1236.

[21] D. N. Dybtsev, M. P. Yutkin, E. V. Peresypkina, A. V. Virovets, C. Serre, G. Férey, V. P. Fedin, *Inorg. Chem.* **2007**, *46*, 6843–6845.

[22] O. K. Farha, C. D. Malliakas, M. G. Kanatzidis, J. T. Hupp, *J. Am. Chem. Soc.* **2010**, *132*, 950–952.

[23] B.-Q. Ma, K. L. Mulfort, J. T. Hupp, *Inorg. Chem.* **2005**, *44*, 4912–4914.

[24] T.-C. Chen, M.-J. Tsai, J.-Y. Wu, *Chem. Eur. J.* **2019**, *25*, 1337–1344.

[25] H. Chung, P. M. Barron, R. W. Novotny, H.-T. Son, C. Hu, W. Choe, *Cryst. Growth Des.* **2009**, *9*, 3327–3332.

[26] K. Maity, K. Nath, M. A. Sinnwell, R. K. Motkuri, P. K. Thallapally, K. Biradha, *Chem. Eur. J.* **2019**, *25*, 14500–14505.

[27] B. Tahmouresilerd, M. Moody, L. Agogo, A. F. Cozzolino, *Dalton Trans.* **2019**, *48*, 6445–6454.

[28] S. V. Bhosale, C. H. Jani, S. J. Langford, *Chem. Soc. Rev.* **2008**, *37*, 331–342.

[29] M. Pan, X.-M. Lin, G.-B. Li, C.-Y. Su, *Coord. Chem. Rev.* **2011**, *255*, 1921–1936.

[30] H. Cao, V. Chang, R. Hernandez, M. D. Heagy, *J. Org. Chem.* **2005**, *70*, 4929–4934.

[31] Y. Takashima, V. M. Martínez, S. Furukawa, M. Kondo, S. Shimomura, H. Uehara, M. Nakahama, K. Sugimoto, S. Kitagawa, *Nat. Commun.* **2011**, *2*, 168–175.

[32] J.-J. Liu, Y. Wang, Y.-J. Hong, M.-J. Lin, C.-C. Huang, W.-X. Dai, *Dalton Trans.* **2014**, *43*, 17908–17911.

[33] M.-J. Tsai, C.-Y. Li, J.-Y. Wu, *CrystEngComm* **2018**, *20*, 6762–6774.

[34] A. L. Spek, *Acta Crystallogr. Sect. D* **2009**, *65*, 148–155.

[35] Z. Chen, S. Xiang, D. Zhao, B. Chen, *Cryst. Growth Des.* **2009**, *9*, 5293–5296.

[36] K. V. Kumar, C. Valenzuela-Calahorro, J. M. Juarez, M. Molina-Sabio, J. Silvestre-Albero, F. Rodriguez-Reinoso, *Chem. Eng. J.* **2010**, *162*, 424–429.

[37] P. Kanoo, R. Matsuda, R. Kitaura, S. Kitagawa, T. K. Maji, *Inorg. Chem.* **2012**, *51*, 9141–9143.

[38] X. Sun, S. Yao, G. Li, L. Zhang, Q. Huo, Y. Liu, *Inorg. Chem.* **2017**, *56*, 6645–6651.

[39] N. Nijem, H. Wu, P. Canepa, A. Marti, K. J. Balkus Jr, T. Thonhauser, J. Li, Y. J. Chabal, *J. Am. Chem. Soc.* **2012**, *134*, 15201–15204.

[40] T.-R. Lin, C.-H. Lee, Y.-C. Lan, S. Mendiratta, L.-L. Lai, J.-Y. Wu, K.-M. Chi, K.-L. Lu, *Polymers* **2018**, *10*, 1398.

[41] A. Schneemann, P. Vervoorts, I. Hante, M. Tu, S. Wannapaiboon, C. Sternemann, M. Paulus, D. C. F. Wieland, S. Henke, R. A. Fischer, *Chem. Mater.* **2018**, *30*, 1667–1676.

[42] D.-m. Chen, X.-p. Zhang, W. Shi, P. Cheng, *Cryst. Growth Des.* **2014**, *14*, 6261–6268.

[43] X.-L. Hu, F.-H. Liu, H.-N. Wang, C. Qin, C.-Y. Sun, Z.-M. Su, F.-C. Liu, *J. Mater. Chem. A* **2014**, *2*, 14827–14834.

[44] X.-L. Hu, Q.-H. Gong, R.-L. Zhong, X.-L. Wang, C. Qin, H. Wang, J. Li, K.-Z. Shao, Z.-M. Su, *Chem. Eur. J.* **2015**, *21*, 7238–7244.

[45] S. Bureekaew, H. Sato, R. Matsuda, Y. Kubota, R. Hirose, J. Kim, K. Kato, M. Takata, S. Kitagawa, *Angew. Chem. Int. Ed.* **2010**, *49*, 7660–7664; *Angew. Chem.* **2010**, *122*, 7826–7830.

[46] S. Sen, S. Neogi, A. Aijaz, Q. Xu, P. K. Bharadwaj, *Inorg. Chem.* **2014**, *53*, 7591–7598.

[47] W. Yang, X. Lin, A. J. Blake, C. Wilson, P. Hubberstey, N. R. Champness, M. Schröder, *Inorg. Chem.* **2009**, *48*, 11067–11078.

[48] M. Arıcı, O. Z. Yeşilel, M. Tas, H. Demiral, H. Erer, *Cryst. Growth Des.* **2016**, *16*, 5448–5459; DOI: 10.1021/acs.cgd.6b00912.

[49] R. Zou, P.-Z. Li, Y.-F. Zeng, J. Liu, R. Zhao, H. Duan, Z. Luo, J.-G. Wang, R. Zou, Y. Zhao, *Small* **2016**, *12*, 2334–2343.

[50] J. Wang, J. Zhang, F. Jin, Y. Luo, S. Wang, Z. Zhang, Y. Wu, H. Liu, J. Y. Lu, M. Fang, *CrystEngComm* **2015**, *17*, 5906–5910.

[51] S. S. Dhankhar, M. Kaur, C. M. Nagaraja, *Eur. J. Inorg. Chem.* **2015**, 5669–5676.

[52] M. Deng, F. Yang, P. Yang, Z. Li, J. Sun, Y. Yang, Z. Chen, L. Weng, Y. Ling, Y. Zhou, *Cryst. Growth Des.* **2015**, *15*, 5794–5801.

[53] Y. Zhao, H. Wu, T. J. Emge, Q. Gong, N. Nijem, Y. J. Chabal, L. Kong, D. C. Langreth, H. Liu, H. Zeng, J. Li, *Chem. Eur. J.* **2011**, *17*, 5101–5109.

[54] J. L. C. Rowsell, O. M. Yaghi, *J. Am. Chem. Soc.* **2006**, *128*, 1304–1315.

[55] K. Sumida, D. L. Rogow, J. A. Mason, T. M. McDonald, E. D. Bloch, Z. R. Herm, T.-H. Bae, J. R. Long, *Chem. Rev.* **2012**, *112*, 724–781.

[56] A. Demessence, D. M. D'Alessandro, M. L. Foo, J. R. Long, *J. Am. Chem. Soc.* **2009**, *131*, 8784–8786.

[57] R. Vaidhyanathan, S. S. Iremonger, G. K. Shimizu, P. G. Boyd, S. Alavi, T. K. Woo, *Science* **2010**, *330*, 650–653.

[58] B. Zheng, J. Bai, J. Duan, L. Wojtas, M. J. Zaworotko, *J. Am. Chem. Soc.* **2011**, *133*, 748–751.

[59] T. M. McDonald, W. R. Lee, J. A. Mason, B. M. Wiers, C. S. Hong, J. R. Long, *J. Am. Chem. Soc.* **2012**, *134*, 7056–7065.

[60] C.-H. Lee, H.-Y. Huang, Y.-H. Liu, T.-T. Luo, G.-H. Lee, S.-M. Peng, J.-C. Jiang, I. Chao, K.-L. Lu, *Inorg. Chem.* **2013**, *52*, 3962–3968.

[61] C.-H. Lee, J.-Y. Wu, G.-H. Lee, S.-M. Peng, J.-C. Jiang, K.-L. Lu, *Inorg. Chem. Front.* **2015**, *2*, 477–484.

[62] A. M. Fracaroli, H. Furukawa, M. Suzuki, M. Dodd, S. Okajima, F. Gándara, J. A. Reimer, O. M. Yaghi, *J. Am. Chem. Soc.* **2014**, *136*, 8863–8866.

[63] S.-D. Liu, B.-C. Kuo, Y.-W. Liu, J.-Y. Lee, K. Y. Wong, H. M. Lee, *CrystEngComm* **2014**, *16*, 8874–8884.

[64] B.-Q. Song, C. Qin, Y.-T. Zhang, X.-S. Wu, L. Yang, K.-Z. Shao, Z.-M. Su, *Dalton Trans.* **2015**, *44*, 18386–18394.

[65] X. Zheng, L. Zhou, Y. Huang, C. Wang, J. Duan, L. Wen, Z. Tian, D. Li, *J. Mater. Chem. A* **2014**, *2*, 12413–12422.

[66] J.-F. Song, J.-J. Luo, Y.-Y. Jia, L.-D. Xin, Z.-Z. Lin, R.-S. Zhou, *RSC Adv.* **2017**, *7*, 36575–36584.

[67] Y.-T. Yan, W.-Y. Zhang, F. Zhang, F. Cao, R.-F. Yang, Y.-Y. Wang, L. Hou, *Dalton Trans.* **2018**, *47*, 1682–1692.

[68] V. Sharma, D. De, S. Pal, P. Saha, P. K. Bharadwaj, *Inorg. Chem.* **2017**, *56*, 8847–8855.

[69] M. E. Germain, T. R. Vargo, B. A. McClure, J. J. Rack, P. G. Van Patten, M. Odol, M. J. Knapp, *Inorg. Chem.* **2008**, *47*, 6203–6211.

[70] R. Fu, S. Hu, X. Wu, *J. Mater. Chem. A* **2017**, *5*, 1952–1956.

[71] H. He, S.-H. Chen, D.-Y. Zhang, E.-C. Yang, X.-J. Zhao, *RSC Adv.* **2017**, *7*, 38871–38876.

[72] X. Wang, P. Yan, Y. Li, G. An, X. Yao, G. Li, *Cryst. Growth Des.* **2017**, *17*, 2178–2185.

[73] S. Wang, T. Cao, H. Yan, Y. Li, J. Lu, R. Ma, D. Li, J. Dou, J. Bai, *Inorg. Chem.* **2016**, *55*, 5139–5151.

[74] D. Singh, C. M. Nagaraja, *Dalton Trans.* **2014**, *43*, 17912–17915.

[75] G.-Y. Wang, L.-L. Yang, Y. Li, H. Song, W.-J. Ruan, Z. Chang, X.-H. Bu, *Dalton Trans.* **2013**, *42*, 12865–12868.

[76] T. K. Kim, J. H. Lee, D. Moon, H. R. Moon, *Inorg. Chem.* **2013**, *52*, 589–595.